 CMES, vol.63, no.1, pp.47-77, 2010

An Improved Unsplit and Convolutional Perfectly Matched Layer Absorbing Technique for the Navier-Stokes Equations Using Cut-Off Frequency Shift

Roland Martin[1] **and Carlos Couder-Castaneda**[1]

Abstract: We develop an unsplit convolutional perfectly matched layer (CPML) technique to absorb efficiently compressible viscous flows and their related supersonic or subsonic regimes at the outer boundary of a distorted computational domain. More particularly subsonic outgoing flows or subsonic wall-boundary layers close to the PML are well absorbed, which is difficult to obtain without creating numerical instabilities over long time periods. This new PML (CPML) introduces the calculation of auxiliary memory variables at each time step and allows an unsplit formulation of the PML. Damping functions involving a high shift in the frequency domain allow a much better absorption of the flow than for cases with no shift or low frequency shifts. The CPML has demonstrated its convenience because the time evolution of damping mechanisms do not need to be split and only the space derivatives of fluxes and primitive variables (velocities and temperature) need to be stored at each time step, reducing by this mean the number of computational arrays used in the numerical code. The results obtained show that CPML can absorb efficiently the out-going subsonic and supersonic fluxes at the outlet condition with very few reflections propagating back into the main domain.

The Navier-Stokes equations are applied in an extremely wide variety of industrial processes and geophysical flow simulations. As an example of interest for the industry, CPML is applied to the particular case of a critical air ejector-diffuser simulation in which the flow propagates along a converging-diverging tube, one main goal being for instance to obtain an efficient tool to model numerically different diffuser designs. In this context we investigate the impact of the PML on an unsteady flow submitted to supersonic expansion at the end of the ejector-diffuser while it remains subsonic in the wall-boundary layer. The numerical integration of the whole system of equations introduces a two-step predictor-corrector time-stepping scheme and a finite difference spatial discretization using a curvilinear

[1] Université de Pau et des Pays de l'Adour, CNRS and INRIA Magique-3D. Laboratoire de Modélisation et Imagerie en Géosciences UMR CNRS 5212, Avenue de l'Université, 64013 Pau cedex, France. E-mail:roland.martin@univ-pau.fr

coordinates transformation that is adapted to the ejector geometry. In this distorted mesh, the spatial finite difference scheme involves a backward-forward discretization and the CPML is able to deal with the distorted mesh in the direction parallel to the base of the PML layer.

Keywords: Convolutional Perfectly Matched Layers, Navier-Stokes, compressible viscous flows, absorbing boundary conditions, supersonic flow, subsonic fow, gas ejector, curvilinear coordinates.

1 Introduction

The development of efficient non-reflecting boundary conditions is a critical problem in all computational fluid codes (CFD) in which subsonic and critical supersonic outlets are involved. These conditions can be introduced for instance in shallow water equations, pollutants transport, geophysical or industrial flows. Many efforts have been devoted to truncate efficiently an infinite medium with absorbing boundary conditions using non-reflecting boundaries based on the method of characteristics (Thompson, 1987, 1990) or NSCBC (Navier-Stokes characteristic boundary conditions) techniques (Poinsot and Lele, 1992) applied to the Navier-Stokes equations. But some discrepancies are coming back from the boundaries into the computational domain due to the non-optimal absorption of flows impinging the out-going boundaries at all angles and not only at angles orthogonal to the boundary. Then other damping conditions like the Perfectly Matched Layer techniques that have been firstly developped for linear equations like Maxwell's equations (Bérenger, 1994; Chew and Weedon, 1994) or elastodynamic equations (Chew and Liu, 1996; Collino and Tsogka, 2001; Bécache, Fauqueux, and Joly, 2003) have been extended to linearized or non-linear formulations of fluid dynamics equations like the shallow water, the Euler or the Navier-Stokes equations (Hesthaven, 1998; Hu, 2001; Hagstrom, 2003; Hu, 2005; Hu, Li, and Lin, 2008). The importance of the PML technique lies in the fact that the absorbing zone is theoretically reflectionless for multi-dimensional linear waves at any angle of incidence and any frequency. The Perfectly Matched Layer (PML) technique consists in constructing absorbing conditions that can absorb efficiently the out-going flux for open boundary conditions and are perfectly matched at the base of the PML with zero reflection coefficient before discretization and very small reflection coefficient after discretization.

In the last decade, substantial progress has been made in the development of the PML technique for the linearized or nonlinear shallow water, Euler or Navier-Stokes equations, starting with the studies for cases with constant mean flows, followed by extensions to cases with non-uniform mean flows. Indeed, in the case

of the linearized shallow-water equations (Navon, Neta, and Hussaini, 2004) have developed a split PML formulation which introduces an explicit finite-difference discretization scheme and a 9-point Laplacian filter to stabilize possible split PML unstable solutions. Furthermore, in the context of computational fluid dynamics, the stabilization of the PML conditions was formerly studied for the linearized Euler equations in (Hu, 2001, 2005) and in (Hagstrom, 2003; Hu, Li, and Lin, 2008) for more general flows described by compressible Navier-Stokes equations. In (Hu, 2001, 2005; Hagstrom, 2003), a change of coordinate in the complex spatial domain is applied in the direction normal to the boundary to avoid unstable solutions. The normal-derivatives in the Euler system are then replaced by an operator which is still differential in the normal direction but pseudo-differential in the other variables. Nataf has developped another stable PML formulation (Nataf, 2006) for the Euler equation. In this new strategy a Smith factorization is applied to the Euler equations in order to separate the propagative and the transport parts of the solution. In this formulation the modes that could produce reflections are damped and consequently the vorticity modes, which satisfy transparent conditions (Lie, 2001) on the outer absorbing boundaries, are not damped, providing a stable scheme for the PML by this mean.

More recently, applications of PML to linearized Navier-Stokes equations and nonlinear Navier-Stokes equations have been discussed (Hu, Li, and Lin, 2008). Although the PML technique itself is relatively simple when it is viewed as a complex change of variables in the frequency domain, it is important to note that, for the PML technique to yield stable absorbing boundary conditions, the phase and group velocities of the physical waves supported by the governing equations must be consistent and in the same direction. Furthermore split PML formulations are essentially introduced in these applications and special treatment needs to be performed to improve absorption of the waves or the different flows that impinge the base of the PML at grazing incidence and travel inside the PML over long time periods.

In order to improve the PML we use a Convolutional formulation of the Perfectly Matched Layer called CPML that has proven to be efficient in elastic wave propagation to absorb surface waves as well as body waves impinging and/or travelling along the PML at non grazing incidence (Komatitsch and Martin, 2007). A shift in the frequency is introduced in the stretching function defining the CPML and acts as a second order Butterworth-like filter. It allows to mimick a non-linear stretching of the mesh in the PML region and to damp non linearly the waves composing the flow when it enters inside the PML at angles different from zero (i.e. non orthogonally to the base of the PML). This CPML technique has proven to be effective in time-evolution equations due to the damping mechanisms that do not need to be split.

Only the space derivatives of primitive variables and fluxes (velocities and stresses) need to be stored at each time step. CPML has also proven to be efficient for more complex rheologies like poroelastic (Martin, Komatitsch, and Ezziani, 2008) or viscoelastic media (Martin and Komatitsch, 2009) using fourth-order finite-difference spatial discretization, or in distorted heterogeneous anisotropic thin slices in presence of a topography using high order finite-element (spectral element) methods (Martin, Komatitsch, and Gedney, 2008). Hence, it is possible to use an unsplit convolutional PML (CPML) for finite-difference or finite-element discretization to improve the computational efficiency of the PML and to reduce this way the number of computational arrays involved in the calculations and therefore the memory storage of all the variables involved in the PML regions. This is another reason to retain these advantages of the CPML and to extend them to the compressible viscous Navier-Stokes equations.

Here the main goal is to show that the CPML conditions can be applied to different regimes of a compressible flow dynamics in which both subsonic to supersonic flows propagate in a distorted mesh ended by optimized and stable PML (see Figures 2 and 3). In a first approach the flow is considered as a subsonic-supersonic slightly diverging directed flow, configuration which allows us to validate our PMLs in a distorted mesh configuration. For instance a converging-diverging nozzle flow is studied here and the particular industrial configuration of a steam ejector is chosen. Figure (1) shows the ejector parts commonly used in the petroleum industry. Indeed, steam jet ejectors offer a simple, reliable, low-cost way to produce vacuum. They are particularly more effective in the chemical industry where an on-site supply of the high-pressure motive gas is available. The ejector operation consists of a high-pressure motive gas that enters the steam chest at low velocity and expands through the converging-diverging nozzle. These results show a decrease in pressure and an increase in velocity, which allows the fluid to enter in the suction inlet at high velocity. The motive fluid, which is now at high velocity, enters and combines with the suction fluid.

Ejector operations are classified as critical or noncritical flow mode. In the critical mode the incoming flow is supersonic, which is the case here in this study. Of course this is not restricted to this application and can be applied to many other applications in which distorted meshes are present. Ejectors classified as critical mean that the fluid velocity in the diffuser throat is always supersonic except in the wall-boundary layers where flows evolve from supersonic to subsonic regime close to the walls due to the non-slip (zero velocity) condition imposed at these walls. As an example we investigate the behavior of a supersonic air flow injected with a Mach number value of 2.0 at the inlet of the diffuser and more particularly its behavior close to the outlet of the ejector where CPML is implemented (see

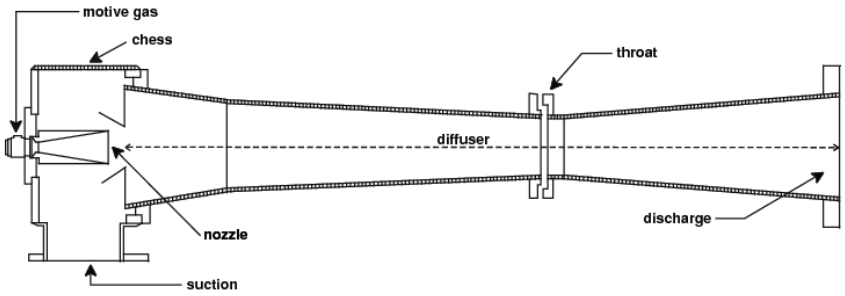

Figure 1: Different parts of the ejector device. We are interested in simulating the diffuser, its nozzle inlet and discharge outlet.

Figure 2).

2 The Governing Equations

We consider the two-dimensional compressible nonlinear Navier-Stokes equation written in the conservation form as:

$$\frac{\partial U}{\partial t}+\frac{\partial F}{\partial x}+\frac{\partial G}{\partial y}=0. \tag{1}$$

The vector U represents the density, the x and y-momenta and the specific internal energy density, and the fluxes F and G are column vectors. U, F and G are defined as:

$$U=\begin{cases}\rho\\ \rho u\\ \rho v\\ \rho e\end{cases} \tag{2}$$

$$F=\begin{cases}\rho u\\ \rho uv+p-\tau_{xx}\\ \rho uv-\tau_{xy}\\ \rho u\left(e+\frac{u^2+v^2}{2}\right)+pu-u\tau_{xx}-v\tau_{xy}+q_x\end{cases} \tag{3}$$

$$G=\begin{cases}\rho v\\ \rho uv-\tau_{xy}\\ \rho v^2+p-\tau_{yy}\\ \rho v\left(e+\frac{u^2+v^2}{2}\right)+pv-u\tau_{xy}-v\tau_{yy}+q_y.\end{cases} \tag{4}$$

The variable ρ represents the density, u and v the horizontal and vertical components of the velocity, p the thermodynamic pressure, e the specific internal energy, $\tau_{i,j}$ (with i and j representing x or y) the components of the newtonian viscous stress tensor, and q_i (with subscript i being equal to x or y) the components of the diffusive heat flux.

For a perfect gas, it is possible to replace e by its expression $\frac{u^2+v^2}{2} + \frac{p}{(\gamma-1)\rho}$ where γ is the isentropic exponent. For more clarity in the calculations, each element of the vector U can be denoted by

$$\begin{aligned} U_1 &= \rho, \\ U_2 &= \rho u, \\ U_3 &= \rho v, \\ U_4 &= \tfrac{\gamma}{\gamma-1} p + \tfrac{u^2+v^2}{2}\rho \end{aligned} \tag{5}$$

and the elements of the column vector F by:

$$\begin{aligned} F_1 &= \rho u, \\ F_2 &= \rho u^2 + p - \tau_{xx}, \\ F_3 &= \rho uv - \tau_{xy}, \\ F_4 &= \tfrac{\gamma}{\gamma-1} pu + \rho u \tfrac{u^2+v^2}{2} - u\tau_{xx} - v\tau_{xy} + q_x. \end{aligned} \tag{6}$$

Also, the elements of the column vector G are denoted by:

$$\begin{aligned} G_1 &= \rho v, \\ G_2 &= \rho uv - \tau_{xy}, \\ G_3 &= \rho v^2 + p - \tau_{yy}, \\ G_4 &= \tfrac{\gamma}{\gamma-1} pv + \rho v \tfrac{u^2+v^2}{2} - u\tau_{xy} - v\tau_{yy} + q_y. \end{aligned} \tag{7}$$

The viscous stress terms are written in terms of velocity derivatives as:

$$\begin{aligned} \tau_{xy} &= \mu \left(\tfrac{\partial u}{\partial y} + \tfrac{\partial v}{\partial x} \right), \\ \tau_{xx} &= \lambda \left(\tfrac{\partial u}{\partial x} + \tfrac{\partial v}{\partial y} \right) + 2\mu \left(\tfrac{\partial u}{\partial x} \right), \\ \tau_{yy} &= \lambda \left(\tfrac{\partial u}{\partial x} + \tfrac{\partial v}{\partial y} \right) + 2\mu \left(\tfrac{\partial v}{\partial y} \right). \end{aligned} \tag{8}$$

where μ is the dynamic viscosity and $\lambda = 2/3\mu$ the second viscosity. Likewise, the components of the heat flux vector (from Fourier's heat law) are defined as:

$$\begin{aligned} q_x &= -k \tfrac{\partial T}{\partial x}, \\ q_y &= -k \tfrac{\partial T}{\partial y}. \end{aligned} \tag{9}$$

The variations of the dynamic viscosity and the thermal conductivity are considered temperature-dependent and they are computed by the following Sutherland's laws as:

$$\mu(T) = \mu_0 \left(\frac{T}{T_0}\right)^{\frac{3}{2}} \frac{T_0 + S}{T + S} \tag{10}$$

and

$$k(T) = \frac{\mu(T)\gamma R}{(\gamma - 1)\,\mathrm{Pr}}. \tag{11}$$

where μ is the viscosity, S the Sutherland temperature and Pr the Prandtl number. In this application the typical values of $T_0 = 273K$, $S = 110.5K$, $\mu_0 = 1.68 \times 10^{-5}$ Pa.s, $\gamma = 1.4$ and $\mathrm{Pr} = 0.71$ are used.

3 The Curvilinear Transformation : example of the ejector diffuser

In the context of directed flows evolving in distorted computational domains we take here the ejector diffuser as an example of application of our PML conditions to the system of equations (1) through equations (2) to (11). To generate the mesh of the ejector diffuser shown in Figure (2), we use a topologically cartesian map from the boundary-fitted coordinate system $(\xi, \eta) \in [0, L] \times [0, 1]$ depicted in the Figure (3) towards the ejector geometry. The lines of constant ξ and η form a rectangular grid in the computational plane (Figure (3)). The following and appropriate curvilinear transformation is then defined as follows

$$\xi = x, \tag{12}$$

$$\eta = \frac{y - y_s(x)}{y_z(x) - y_s(x)} \tag{13}$$

where $y_s(x)$ and $y_z(x)$ are the functions describing respectively the lower and upper walls of the diffuser and are defined in meters as

$$y_s(x) = \begin{cases} 0.0 \text{ for } x \leq 0.1 \\ \frac{8}{167.875}(x - 0.1) \text{ for } 0.1 < x \leq 1.77875 \\ 0.08 \text{ for } 1.77875 < x \leq 2.99125 \\ -\frac{8}{89}(x - 2.99125) + 0.08 \text{ for } x > 2.99125 \end{cases} \tag{14}$$

$$y_z(x) = \begin{cases} 0.42 \text{ for } x \leq 0.1 \\ -\frac{8}{167.875}(x - 0.1) + 0.42 \text{ for } 0.1 < x \leq 1.77875 \\ 0.34 \text{ for } 1.77875 < x \leq 2.99125 \\ \frac{8}{89}(x - 2.99125) + 0.34 \text{ for } x > 2.99125 \end{cases} \tag{15}$$

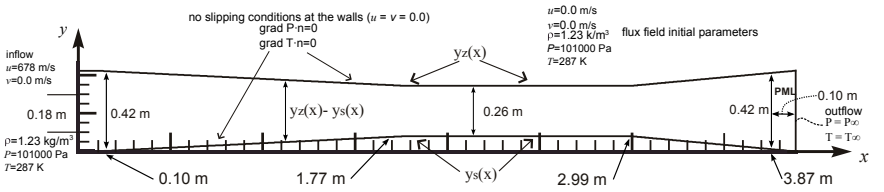

Figure 2: The physical ejector configuration is depicted. The initial conditions are given as well as the kind of inflow, outflow and wall conditions. On the left constant inlet conditions are set for velocity components, temperature and pressure all over the time of simulation. At the upper and lower walls, non-slip velocity conditions are set ($u = v = 0$ m/s) and null pressure and temperature gradients ($\nabla P \cdot n = 0$, and $\nabla T \cdot n = 0$) are imposed any time. At the right end of the 10 to 20 points PML layer, Dirichlet conditions are imposed, that is to say $u = u_\infty = 0$ m/s, $v = v_\infty = 0$ m/s, $P = P_\infty = 0.1$ MPa and $T = T_\infty = 286$ K. These values correspond to initial values inside the diffuser at ambiant atmosphere conditions.

With this transformation, ξ varies from 0 to L (the horizontal length of the diffuser) and η varies from 0.0 (lower wall) to 1.0 (upper wall) in the computational plane. Furthermore, $\eta = 0.0$ corresponds to the lower wall surface in the physical plane and $\eta = 1.0$ corresponds to the upper boundary. The inflow boundary occurs at $\xi = 0$, and the physical outflow boundary is at $\xi = L$. With this transformation, we can adequately handle the compression or expansion waves that are produced in a supersonic flow and fan out from the corners of the breaks-in-slope of the walls, as well as the modelling of the subsonic boundary layers in the vicinity of the lower and upper walls (Couder-Castañeda, 2009). By simplicity we denote the different metrics of the transformation as follows :

$$\begin{aligned} \frac{\partial \xi}{\partial x} &= \xi_x \\ \frac{\partial \xi}{\partial y} &= \xi_y \\ \frac{\partial \eta}{\partial x} &= \eta_x \\ \frac{\partial \eta}{\partial y} &= \eta_y. \end{aligned} \tag{16}$$

These metrics are defined by the derivatives of the equations (12) and (13) as follows: $\xi_x = 1$, $\xi_y = 0$, $\eta_x = \frac{1}{y_z(x) - y_s(x)}$, $\eta_y = \frac{\eta\left[y'_s(x) - y'_z(x)\right] - y'_s(x)}{y_z(x) - y_s(x)}$. The global system of

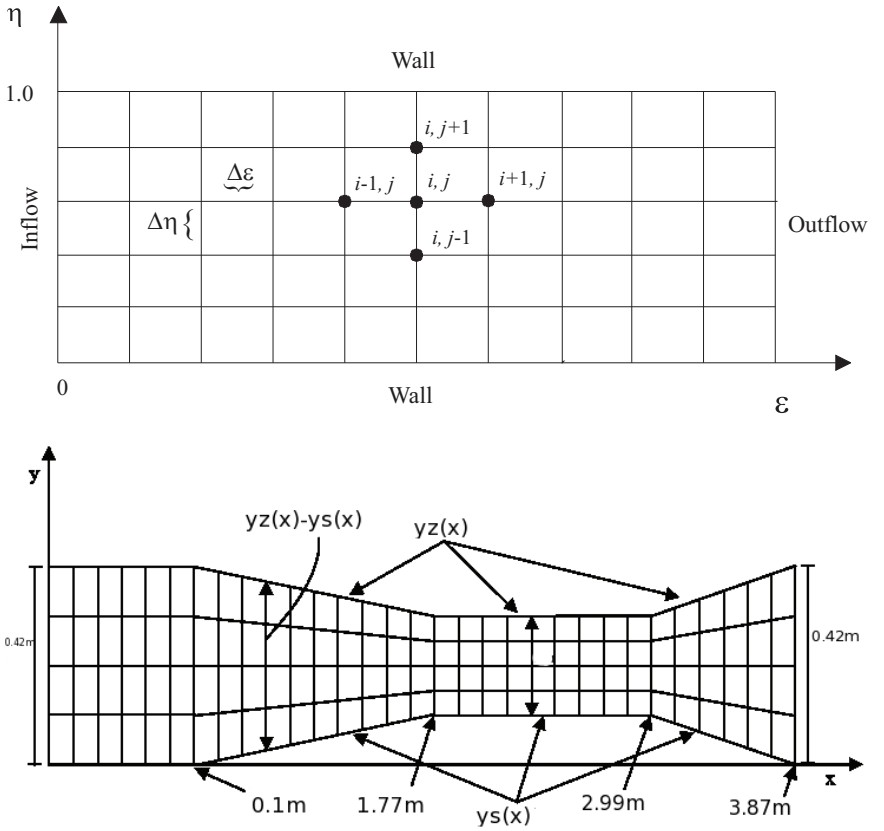

Figure 3: We show the reference computational frame (top) and its (ξ,η) system of coordinates that are mapped to the distorted mesh (bottom) of the ejector-diffuser configuration depicted in Figure (2).

equations (1) is then reformulated as:

$$\begin{aligned}
Continuity: \quad & \frac{\partial U_1}{\partial t} = -\left[\frac{\partial F_1}{\partial \xi}\xi_x + \frac{\partial F_1}{\partial \eta}\eta_x\right] - \left[\frac{\partial G_1}{\partial \eta}\eta_y\right] \\
Momentum\ x: \quad & \frac{\partial U_2}{\partial t} = -\left[\frac{\partial F_2}{\partial \xi}\xi_x + \frac{\partial F_2}{\partial \eta}\eta_x\right] - \left[\frac{\partial G_2}{\partial \eta}\eta_y\right] \\
Momentum\ y: \quad & \frac{\partial U_3}{\partial t} = -\left[\frac{\partial F_3}{\partial \xi}\xi_x + \frac{\partial F_3}{\partial \eta}\eta_x\right] - \left[\frac{\partial G_3}{\partial \eta}\eta_y\right] \\
Energy: \quad & \frac{\partial U_4}{\partial t} = -\left[\frac{\partial F_4}{\partial \xi}\xi_x + \frac{\partial F_4}{\partial \eta}\eta_x\right] - \left[\frac{\partial G_4}{\partial \eta}\eta_y\right]
\end{aligned} \tag{17}$$

4 The CPML formulation

In our previous articles on the unsplit perfectly matched layer formulation for the first-order system of elastic wave equations we performed a convolution integration (Komatitsch and Martin, 2007; Martin, Komatitsch, and Ezziani, 2008; Martin, Komatitsch, and Gedney, 2008; Martin and Komatitsch, 2009) of the memory variable equations (CPML formulation) following the recursive convolution procedure of Luebbers and Hunsberger (1992). Now we summarize briefly the extension of this technique to the Navier-Stokes equation. As in the construction of a classical PML or a Convolution PML, the spatial derivatives along the axis perpendicular to the PML layer, say x, are rewritten in a stretched coordinate $\tilde{x}$, based on (see e.g. Komatitsch and Martin (2007)):

$$\partial_{\tilde{x}} = \frac{1}{s_x}\partial_x \tag{18}$$

where

$$s_x = \kappa_x + \frac{d_x}{\alpha_x + i\omega}. \tag{19}$$

ω means the angular frequency equal to πf, f being the frequency and α_x is a shift in the frequency domain. Then, following Komatitsch and Martin (2007), we can express:

$$\frac{1}{s_x} = \frac{1}{\kappa_x} - \frac{d_x}{\kappa_x^2}\frac{1}{(d_x/\kappa_x + \alpha_x) + i\omega} \tag{20}$$

where

$$\begin{aligned}
d_x &= d_0\left(\frac{x}{L'}\right)^N \\
\kappa_x &= 1 + (\kappa_{\max} - 1)\left(\frac{x}{L'}\right)^m \\
\alpha_x &= \alpha_{\max}[1 - (x/L')^p].
\end{aligned} \tag{21}$$

d_x is the damping function profile, κ_x is the stretching function always greater than 1 and α_x is the shift in the frequency domain. $L' = L\Delta x$ is the thickness of the PML layer, L the number of points inside the PML in the x direction, $N = 2$ and $d_0 = -\frac{(N+1)V_{\max}\log(R_c)}{2L'}$. $V_{\max}$ is taken equal to the maximum eigenvalue of the convection part i.e. $V_{\max} = \max(|U\cdot\tilde{n}|, |U\cdot\tilde{n}-c|, |U|)$ where $\tilde{n}$ is the normal evaluated on each cell edge and Δh is the minimal distance between all nodes of each spatial cell. U is the velocity vector and c is the sound speed. R_c is the target theoretical reflection coefficient, chosen here as 0.1% (see e.g. Collino and Tsogka (2001)) and c is the sound speed. Without lack of generallity we can chose $V_{\max}$ as $c_o(1+M_o)$ where c_o is the maximum sound speed and M_o is the maximum Mach number that is equal to $\frac{|u_o|}{c_o}$, u_o being the maximum velocity.

In the function $\alpha_x \geq 0$ we also take $p = 1$ and $\alpha_{\max} = \pi f_c$ which is a cut-off frequency of the chosen numerical scheme for the grid spatial step Δx. While in Komatitsch and Martin (2007) f_c represents the dominant frequency of the seismic source that injects energy in the elastic media, here f_c represents a frequency related to the mesh resolution used in the numerical integration of the Navier-Stokes equations. f_c is chosen such that it verifies the inequality $n_{PW} \leq \text{Min}\left(\frac{|U\cdot\tilde{n}+c|}{\pi\Delta h}, \frac{|U\cdot\tilde{n}+c|}{\pi\Delta h}, \frac{|U\cdot\tilde{n}|}{\pi\Delta h}\right)$ where n_{PW} is the number of points per minimal wavelength for the considered spatial numerical scheme. $\kappa_{\max}$ usually lies between 1 and 20 (Martin and Komatitsch, 2009) and we usually take $m = 2$. At the right end of the PML layer a Dirichlet condition is imposed for velocity components, temperature and pressure : during all the simulation velocity components are set to zero there and pressure and temperature are set there to constant values equal to the initial ambiant air values ($u = u_\infty = 0$ m/s, $v = v_\infty = 0$ m/s, $P = P_\infty = 0.1$ MPa and $T = T_\infty = 286$ K respectively).

By sake of simplicity we will study the term $\frac{1}{s_x}\partial_x F_i$ in detail, keeping in mind that similar formulations are derived for the x and y derivatives of u, v and G_i in 2D when PML layers are present along both axes of the grid. The term $\partial_x F_i$ is transformed into

$$\frac{1}{s_x}\partial_x F_i = \frac{1}{\kappa_x}\partial_x F_i - \frac{d_x}{\kappa_x^2}\frac{1}{(d_x/\kappa_x+\alpha_x)+i\omega}\partial_x F_i \tag{22}$$

and let us denote $\Psi_x(F_i)$ the auxiliary memory variable associated with $\partial_x F_i$, i.e.:

$$\Psi_x(F_i) = -\frac{d_x}{\kappa_x^2}\frac{1}{(d_x/\kappa_x+\alpha_x)+i\omega}\partial_x F_i\,. \tag{23}$$

In order to reformulate the above equation in the time domain we retain here the idea of the convolutional PML (CPML) technique developed in the elastodynamic case by Komatitsch and Martin (2007). By sake of simplicity we state that $\partial_{\tilde{x}}$ is the

inverse Fourier transform of equation (18) from the frequency domain to the time domain. Denoting by $\bar{s}_x(t)$ the inverse Fourier transform of $\frac{1}{s_x}$, ∂_x is then replaced by:

$$\partial_{\tilde{x}} = \bar{s}_x(t) * \partial_x \tag{24}$$

After calculating the expression of $\bar{s}_x(t)$ and after some algebraic operations (see equations (17) and (18) in Komatitsch and Martin (2007)), we obtain

$$\partial_{\tilde{x}} = \frac{1}{\kappa_x}\partial_x + \zeta_x(t) * \partial_x. \tag{25}$$

with

$$\zeta_x(t) = -\frac{d_x}{\kappa_x^2} H(t)\, e^{-(d_x/\kappa_x+\alpha_x)t}, \tag{26}$$

where H is the Heaviside distribution. As we have null initial conditions, the convolution term at time step n can be approximated following the recursive convolution method of Luebbers and Hunsberger (1992):

$$\Psi_x^n = (\zeta_x * \partial_x)^n \simeq \sum_{m=0}^{N-1} Z_x(m)\,(\partial_x)^{n-(m+1/2)} \tag{27}$$

with:

$$Z_x(m) = -\frac{d_x}{\kappa_x^2}\int_{m\Delta t}^{(m+1)\Delta t} e^{-(d_x/\kappa_x+\alpha_x)\tau}\,\mathrm{d}\tau = a_x e^{-(d_x/\kappa_x+\alpha_x)m\Delta t}. \tag{28}$$

Setting

$$b_x = e^{-(d_x/\kappa_x+\alpha_x)\Delta t} \qquad \text{and} \qquad a_x = \frac{d_x}{\kappa_x(d_x+\kappa_x\alpha_x)}(b_x-1) \tag{29}$$

and developing $Z_x(m)$ in equation (27), the convolution term can be viewed as a recursive sum. Therefore, we can update the memory variable Ψ_x of the derivative of variable f (velocity components u and v, temperature and fluxes F_i and G_i) along direction x at each time step based on

$$\Psi_x^{n+1}(f) = b_x \Psi_x^n(f) + a_x\,(\partial_x f)^{n+1/2}. \tag{30}$$

If we use a second-order two-steps (called also predictor-corrector) time scheme discretization of equation (30) in the time domain, $\Psi_x^{F_i}$ satisfies

$$\Psi_x^{F_i}((n+\nu_i)\Delta t) \quad = \quad b_{x,i}\Psi_x^{F_i}(n\Delta t) + a_{x,i}\partial_x F_i((n+\nu_i)\Delta t) \tag{31}$$

with

$$b_{x,i} = e^{-(d_x/\kappa_x+\alpha_x)\nu_i\Delta t} \qquad \text{and} \qquad a_{x,i} = \frac{d_x}{\kappa_x(d_x+\kappa_x\alpha_x)}(b_{x,i}-1) \tag{32}$$

where subscript i corresponds to the ith iteration of a given predictor-corrector time-stepping scheme. Here i takes values 1 or 2 because we are at the second order in time and ν_i is a fraction of the time step that takes values $\nu_1 = 0.5$ and $\nu_2 = 1$. This can be reformulated at higher orders in time following Martin, Komatitsch, Gedney, and Bruthiaux (2010). In the next section this time discretization is described for the whole set of equations and not only for the time evolution equations of the memory variables.

5 Application of CPML to the Navier-Stokes equation

The CPML formulation described in the previous section can be easily implemented in an existing finite-difference code without PML by simply replacing the spatial derivatives ∂_x with $\frac{1}{\kappa_x}\partial_x + \Psi_x$ and advancing Ψ_x in time using the same time evolution scheme as for the other variables. If we apply this reformulation of the space derivatives to the whole set of equations and if we perform a curvilinear transformation of the computational domain, the derivatives $\frac{1}{\kappa_x}\partial_x F_i + \Psi_x$ along the x axis are computed according to the chain rule as $\frac{1}{\kappa_x}\left(\partial_\xi F_i \xi_x + \Psi_\xi^{F_i}\xi_x + \partial_\eta F_i \eta_x + \Psi_\eta^{F_i}\eta_x\right)$. So with this idea we can replace the governing equations (17) as follows:

$$\begin{aligned}
\textit{Continuity}: \quad & \frac{\partial U_1}{\partial t} = -\left[\left(\frac{1}{k_x}\frac{\partial F_1}{\partial \xi} + \Psi_\xi^{F_1}\right)(\xi_x) + \left(\frac{1}{k_x}\frac{\partial F_1}{\partial \eta} + \Psi_\eta^{F_1}\right)(\eta_x)\right] \\
& - \left[\left(\frac{1}{k_y}\frac{\partial G_1}{\partial \eta} + \Psi_\eta^{G_1}\right)(\eta_y)\right] \\
\textit{Momentum } x: \quad & \frac{\partial U_2}{\partial t} = -\left[\left(\frac{1}{k_x}\frac{\partial F_2}{\partial \xi} + \Psi_\xi^{F_2}\right)(\xi_x) + \left(\frac{1}{k_x}\frac{\partial F_2}{\partial \eta} + \Psi_\eta^{F_2}\right)(\eta_x)\right] \\
& - \left[\left(\frac{1}{k_y}\frac{\partial G_2}{\partial \eta} + \Psi_\eta^{G2}\right)(\eta_y)\right] \\
\textit{Momentum } y: \quad & \frac{\partial U_3}{\partial t} = -\left[\left(\frac{1}{k_x}\frac{\partial F_3}{\partial \xi} + \Psi_\xi^{F_3}\right)(\xi_x) + \left(\frac{1}{k_x}\frac{\partial F_3}{\partial \eta} + \Psi_\eta^{F_3}\right)(\eta_x)\right] \\
& - \left[\left(\frac{1}{k_y}\frac{\partial G_3}{\partial \eta} + \Psi_\eta^{G_3}\right)(\eta_y)\right] \\
\textit{Energy}: \quad & \frac{\partial U_4}{\partial t} = -\left[\left(\frac{1}{k_x}\frac{\partial F_4}{\partial \xi} + \Psi_\xi^{F_4}\right)(\xi_x) + \left(\frac{1}{k_x}\frac{\partial F_4}{\partial \eta} + \Psi_\eta^{F_4}\right)(\eta_x)\right] \\
& - \left[\left(\frac{1}{k_y}\frac{\partial G_4}{\partial \eta} + \Psi_\eta^{G_4}\right)(\eta_y)\right].
\end{aligned} \tag{33}$$

For the discretization of the viscous stress terms it is also necessary to apply the metrics of the transformation defined by expressions (12), (13) and (16). These viscous stress terms are then expanded as follows:

$$\begin{aligned}
\tau_{xy} &= \mu\frac{\partial u}{\partial \eta}\eta_y + \frac{\mu}{\kappa_x}\left(\frac{\partial v}{\partial \xi} + \frac{\partial v}{\partial \eta}\eta_x\right) + \mu\Psi\left(\frac{\partial v}{\partial x}\right) \\
\tau_{xx} &= \frac{\lambda+2\mu}{\kappa_x}\left(\frac{\partial u}{\partial \xi} + \frac{\partial u}{\partial \eta}\eta_x\right) + \lambda\frac{\partial v}{\partial \eta}\eta_y + (\lambda+2\mu)\Psi\left(\frac{\partial u}{\partial x}\right) \\
\tau_{xx} &= \frac{\lambda}{\kappa_x}\left(\frac{\partial u}{\partial \xi} + \frac{\partial u}{\partial \eta}\eta_x\right) + (\lambda+2\mu)\frac{\partial v}{\partial \eta}\eta_y + \lambda\Psi\left(\frac{\partial u}{\partial x}\right).
\end{aligned} \tag{34}$$

For the heat flux vector the transformation is

$$\begin{aligned}
q_x &= -\frac{k}{\kappa_x}\left(\frac{\partial T}{\partial \xi} + \frac{\partial T}{\partial \eta}\frac{\partial \eta}{\partial x}\right) - k\Psi\left(\frac{\partial T}{\partial x}\right) \\
q_y &= -k\left(\frac{\partial T}{\partial \eta}\eta_y\right).
\end{aligned} \tag{35}$$

According to the previous section (i.e., equation (30)), we can implement the CPML by updating the array variable Ψ for each flux F^i and G_i and each primitive variable u, v or T along the respective direction ξ or η at each time step. In the ξ direction Ψ_x is obtained as follows:

$$\Psi_x^{n+1}(f) = b_x\Psi_x^n(f) + a_x(\partial_x f)^{n+1/2} \tag{36}$$

where variable f can be F^i, G^i, u, v or T and where $b_x = e^{-(d_x/k_x+\alpha_x)\Delta t}$ and $a_x = \frac{d_x}{k_x(d_x+k_x\alpha_x)}(b_x-1)$. In the system of equations (33) we can regroup the memory terms as:

$$\begin{aligned}
\Psi^{F_x^i} &= \Psi^{F_\xi^i}\xi_x + \Psi^{F_\eta^i}\eta_x \\
\Psi^{G_y^i} &= \Psi^{G_\xi^i}\xi_y + \Psi^{G_\eta^i}\eta_y
\end{aligned} \tag{37}$$

and we apply (36) which leads to

$$\Psi_x^{n+1}(F^i) = b_x\Psi_x^n(F^i) + a_x\left(\frac{\partial F^i}{\partial \xi}\xi_x + \frac{\partial F^i}{\partial \eta}\eta_x\right)^{n+1/2} \tag{38}$$

and $\Psi^{G_y^i} = 0$ so $\Psi_y = 0$ because there are no PML layers at the lower and upper walls ($a_y = b_y = 0$).

Furthermore each flux F^i contains viscous stresses and heat diffusion fluxes which involve derivatives of primitive variables u, v and T. The memory variables associated to these viscous stresses and heat fluxes are calculated as follows:

$$\begin{aligned}
\Psi_x^{n+1}(\frac{\partial u}{\partial x}) &= b_x \Psi_x^n(\frac{\partial u}{\partial x}) + a_x(\frac{\partial u}{\partial x})^{n+1/2} \\
\Psi_x^{n+1}(\frac{\partial v}{\partial x}) &= b_x \Psi_x^n(\frac{\partial v}{\partial x}) + a_x(\frac{\partial v}{\partial x})^{n+1/2} \\
\Psi_x^{n+1}(\frac{\partial T}{\partial x}) &= b_x \Psi_x^n(\frac{\partial T}{\partial x}) + a_x(\frac{\partial T}{\partial x})^{n+1/2}
\end{aligned} \tag{39}$$

All these equations must now be solved using a predictor-corrector time-stepping, which is detailed in the following section.

6 The Numerical Scheme

As we can observe in the time evolution equations of memory variables Ψ and the whole set of equations (33), variables Ψ are evaluated at time t^{n+1} while spatial derivatives of F^i and G^i, conservative (U) or primitive (u, v, p and T) variables are evaluated at $t^{n+1/2}$. A second-order predictor-corrector time-stepping scheme is then introduced to deal with these updates of the different variables involved. This time-stepping applied to whole system of equations (33) is formulated as follows:

Predictor:

$$\begin{aligned}
&\Psi_x^{n+1/2}[F^n, S^x(U^n)] = \\
&\qquad b_x \Psi_x^{n-1/2}[F^n, S^x(U^n)] + a_x \left[\frac{1}{\Delta\xi} \left(F_{i+1,j}^n - F_{i,j}^n \right) \xi_x(i,j) + S_{i,j}^x(U_{i,j}^n) \right]
\end{aligned}$$

$$\begin{aligned}
U_{i,j}^* \quad = \quad & U_{i,j}^n - \frac{1}{\kappa_x(i,j)} \frac{\Delta t}{\Delta\xi} \left(F_{i+1,j}^n - F_{i,j}^n \right) \xi_x(i,j) \\
& - \frac{1}{\kappa_x(i,j)} \frac{\Delta t}{\Delta\eta} \left(F_{i,j+1}^n - F_{i,j}^n \right) \eta_x(i,j) - \frac{\Delta t}{\Delta\eta} \left(G_{i,j+1}^n - G_{i,j}^n \right) \eta_y(i,j) \\
& - \frac{\Delta t}{\kappa_x(i,j)} S_{i,j}^x(U_{i,j}^n) - \Delta t S_{i,j}^y(U_{i,j}^n) - \Delta t \Psi_x^{n+1/2}[F^n, S^x(U^n)].
\end{aligned} \tag{40}$$

The artificial viscosities S^x and S^y are introduced to avoid possible oscillations near strong gradients and are given by

$$S_{i,j}^x(U_{i,j}^n) = \frac{C^x \left| p_{i+1,j}^n - 2p_{i,j}^n + p_{i-1,j}^n \right|}{p_{i+1,j}^n + 2p_{i,j}^n + p_{i-1,j}^n} \left(U_{i+1,j}^n - 2U_{i,j}^n + U_{i-1,j}^n \right) \tag{41}$$

and

$$S^y_{i,j}(U^n_{i,j}) = \frac{C^y \left| p^n_{i,j+1} - 2p^n_{i,j} + p^n_{i,j-1} \right|}{p^n_{i,j+1} + 2p^n_{i,j} + p^n_{i,j-1}} \left(U^n_{i,j+1} - 2U^n_{i,j} + U^n_{i,j-1} \right) \tag{42}$$

where the C^x and C^y are two parameters which have typical values ranging from 0.01 to 0.3. They typically scale as Max $\left[(|U| + c)\Delta t \sqrt{\frac{1}{(\Delta x)^2} + \frac{1}{(\Delta y)^2}} \right]$ which is of the order of the CFL stability number value. For this application we let $C^x = C^y = 0.1$.

Corrector:

$$\Psi^{*n+3/2}_x[F^*, S^x(U^*)] = b_x \Psi^{*n+1/2}_x[F^*, S^x(U^*)] + a_x \left[\frac{1}{\Delta\xi} \left(F^*_{i+1,j} - F^*_{i,j} \right) \xi_x(i,j) + S^x_{i,j}(U^*_{i,j}) \right]$$

$$\begin{aligned} U^{n+1}_{i,j} &= \frac{1}{2}[U^n_{i,j} + U^*_{i,j} - \frac{1}{\kappa_x(i,j)} \frac{\Delta t}{\Delta\xi} (F^*_{i+1,j} - F^*_{i,j}) \xi_x(i,j) \\ &\quad - \frac{1}{\kappa_x(i,j)} \frac{\Delta t}{\Delta\eta} (F^*_{i+1,j} - F^*_{i,j}) \eta_x(i,j) - \frac{\Delta t}{\Delta y} (G^*_{i,j+1} - G^*_{i,j}) \eta_y(i,j) \\ &\quad - \frac{\Delta t}{\kappa_x(i,j)} S^x_{i,j}(U^*_{i,j}) - \Delta t \Psi^{*n+3/2}_x[F^*, S^x(U^*)] - \Delta t S^y_{i,j}(U^*_{i,j})]. \end{aligned} \tag{43}$$

By combining the predictor and the corrector systems of equations given above, we retrieve a second order discretization of the equations similar to the discretized equations of the elastodynamics and similar discretized memory variable equations as in equations (36) and (39). Indeed, after developping the corrector scheme, we can rewrite the discretized predictor-corrector system of equations as:

$$\Psi^{n+1}_x[F, S^x]^{n+1/2} = b_x \Psi^{n-1}_x[F, S^x]^{n+1/2} + a_x \left[\frac{1}{\Delta\xi} \left(F^{n+1/2}_{i+1,j} - F^{n+1/2}_{i,j} \right) \xi_x(i,j) + S^x_{i,j}(U^{n+1/2}_{i,j}) \right]$$

$$\begin{aligned} U^{n+1}_{i,j} &= U^n_{i,j} - \frac{1}{\kappa_x(i,j)} \frac{\Delta t}{\Delta\xi} \left(F_{i+1,j} - F_{i,j} \right)^{n+1/2} \xi_x(i,j) \\ &\quad - \frac{1}{\kappa_x(i,j)} \frac{\Delta t}{\Delta\eta} \left(F^n_{i,j+1} - F_{i,j} \right)^{n+1/2} \eta_x(i,j) - \frac{\Delta t}{\Delta y} \left(G_{i,j+1} - G_{i,j} \right)^{n+1/2} \eta_y(i,j) \\ &\quad - \frac{\Delta t}{\kappa_x(i,j)} S^x_{i,j}(U_{i,j})^{n+1/2} - \Delta t S^y_{i,j}(U_{i,j})^{n+1/2} - \Delta t \Psi^{n+1}_x[F, S^x]^{n+1/2} \end{aligned} \tag{44}$$

where

$$\begin{aligned} F^{n+1/2} &= \frac{1}{2}(F^n + F^*) \\ G^{n+1/2} &= \frac{1}{2}(G^n + G^*) \\ S^{xn+1/2} &= \frac{1}{2}(S^{xn} + S^{x*}) \\ S^{yn+1/2} &= \frac{1}{2}(S^{yn} + S^{y*}) \\ \Psi_x^{n+1} &= \frac{1}{2}(\Psi_x^{n+1/2} + \Psi_x^{*n+3/2}). \end{aligned} \tag{45}$$

For the discretization of the viscous stress or thermal diffusive terms we need a weighted derivative of the velocity components u and v or the temperature T in the ξ and η directions. By sake of clarity and to avoid extensive discretized formulations of the derivatives of velocity components and temperature that are involved in stress components and thermal fluxes, we denote by ϕ a variable that can take values of u, v and T. The discretized derivatives of ϕ along ξ and η are written as:

$$\left.\frac{\partial \phi}{\partial \xi}\right|_{i,j} = \frac{\phi_{i+1,j} + \left(\alpha_\xi^2 - 1\right)\phi_{i,j} - \alpha_\xi^2 \phi_{i-1,j}}{\alpha_\xi\left(\alpha_\xi + 1\right)\Delta\xi_i} \tag{46}$$

$$\left.\frac{\partial \phi}{\partial \eta}\right|_{i,j} = \frac{\phi_{i,j+1} + \left(\alpha_\eta^2 - 1\right)\phi_{i,j} - \alpha_\xi^2 \phi_{i,j-1}}{\alpha_\eta\left(\alpha_\eta + 1\right)\Delta\eta_j} \tag{47}$$

where $\alpha_\xi = \dfrac{\Delta\xi_{i+1}}{\Delta\xi_i}$ and $\alpha_\eta = \dfrac{\Delta\eta_{j+1}}{\Delta\eta_j}$. Therefore, we can spatially discretize the viscous stresses and the diffusive heat fluxes given by equations (8) and (9) using these weighted derivatives and replacing ϕ by the velocity components u and v or the temperature T in the decomposed formulations of the fluxes (34) and (35).

Finally, the time step verifies a CFL (Courant-Frederichs-Lewy) stability condition as follows:

$$\mathrm{Max}_{i=(1,N_x),\, j=(1,N_y)}\left[\Delta t\left(\frac{|u_{i,j}|}{\Delta x_{i,j}} + \frac{|v_{i,j}|}{\Delta y_{i,j}} + a_{i,j}\sqrt{\frac{1}{\Delta x_{i,j}^2} + \frac{1}{\Delta y_{i,j}^2}}\right)\right] \leq C, \tag{48}$$

where $C = 0.5$ is a CFL number chosen numerically and $a_{i,j} = \sqrt{\dfrac{\gamma \cdot p_{i,j}}{\rho_{i,j}}}$ is the sound speed in the fluid.

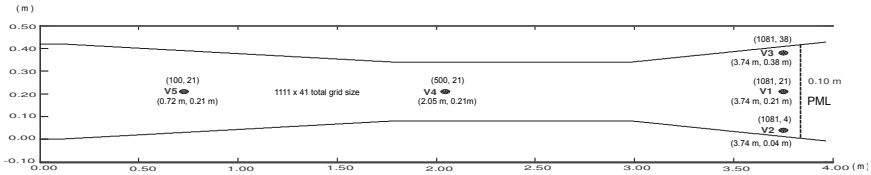

Figure 4: The PML region and the receivers located at five different positions in the ejector-diffuser device are depicted. In this study the PML thickness L' is taken equal to $10\Delta x = 0.1$ m (as in the picture) or $20\Delta x = 0.2$ m for $L = 10$ or 20 points respectively.

7 The Numerical Test

The mesh is generated using the CFL stability criterion (48), the grid size is 1101 $\times$ 41 and two different thicknesses L of the PML with values of 10 or 20 points ($L' = L\Delta x = 10\Delta x$ or $20\Delta x$) are tested in the ξ direction depending on the simulation under study. In what follows, we define a "receiver" as a virtual point that is located somewhere in the computational domain and that stores the evolution of a variable (velocity component, density, pressure, temperature, or other physical variables) during the expected time period of simulation. In Figure (4) the whole domain is depicted with three receivers V_1 ($x = 3.75$, $y = 0.21$), V_2 ($x = 3.75$, $y = 0.04$) and V_3 ($x = 3.75$, $y = 0.38$) located close to the right PML, 20 points from the PML (V_2 and V_3 are located respectively at 3 and 2 points from the lower and upper walls) and with two receivers V_4 ($x = 2.046$, $y = 0.21$) and V_5 ($x = 0.7275$, $y = 0.21$) located on the symmetry axis of the nozzle. The solutions stored at these receivers at each time step are compared to a reference solution computed in a larger computational domain ended by a PML. The flow is initialized in the nozzle at ambiant air conditions with a pressure, a density and a temperature respectively equal to 10^5 Pa, 1.23 Kg/m^3 and 286 K everywhere inside the computational domain as well as at the inflow and outflow boundaries and the velocity field is initialized to $u_o = v_o = 0.0$ m/s inside the nozzle. At the upstream boundary, velocities are initialized to $u_o = 678$ m/s and $v_o = 0.0$ m/s at a vent of 0.18 m. Simulations are performed over 5 s, i.e. 5×10^6 time steps with a time step Δt of 10^{-6} s that verifies criterion (48). The flux reaches a steady state after approximately 4 s of real simulation. Different simulations have been performed here with different values of the frequency shift f_c that we vary from 40 to 100 Hz, and a typical value of κ_{max} equal to 10. The PML thickness is defined with 10 or 20 points and simulations are performed with different values of the reflection coefficient R_c equal to 10^{-3}, 10^{-4} or 10^{-5}. In Figures (5) and (6), snapshots of the Mach number and the density are shown at different times from 0.2 s to 5 s. In this particular case we take

$f_c = 100$ Hz and $R_c = 10^{-5}$ and $L = 20$. We can observe how expected patterns and physical features like compression cells or expansion flows develop respectively at the inner core and at the diverging outlet of the nozzle. The expected diverging and expanded flow structure at the right end of the nozzle is well preserved during all the simulation with no spurious waves or fluxes returning back from the right PML. In this part of the device the density decreases as it should be and the Mach number increases to values around 2.2 with the generation of an expansion fan at the outlet without significant distortions of its structure that could be due to parasit fluxes coming from the PML. In the meantime, the Mach number decreases in the subsonic boundary layer close to the walls without instabilities that could possibly be generated by the presence of the PML. In the case of PML solutions computed with $f_c = 100$ Hz and $R_c = 10^{-5}$ no significant spurious flows are propagating back into the main domain as can be shown in Figure (7) in which velocity solutions with simple and standard Newmann outlet conditions ($\left.\frac{\partial U}{\partial \xi}\right|_{\text{outlet}} = 0$) are compared to solutions with PML conditions at different times. While the velocities are significantly reflected at the outer Newmann boundary, the velocities are not submitted to significant reflections in the case of PML solutions, even near the upper and lower walls in the subsonic boundary layer which is generally difficult to stabilize. When a simple Newmann boundary condition is imposed significant spurious flows are returning back into the computational domain from the outer boundary, which introduces strong oscillations in the solution. Furthermore, these effects are commonly produced when the flux is critical. On the contrary, we can see that we do not have spurious returning flows when PML conditions are used. More precisely, in Figures (7)-(a,c,e) we can see a small shock between the main flow and the non-physical returning flow in the right zoomed region close to the outer boundary in the case of Newmann condition while this situation is not produced in the CPML case (Figures (7)-(b,d,f)). Furthermore, in Figure (8) we also observe in the zoomed region that density contours are efficiently absorbed with few reflections at different times of simulation as well as the flow velocities when CPML is used. In order to analyze the sensitivity of the solutions to different parameters involved in the damping functions, we performed different simulations with varying parameters like the frequency shift f_c, the PML thickness L and the reflection coefficient R_c. In Figures (9), (10) and (11) we show the evolution of the density and the horizontal velocity over 5 million time steps (5 s) at the four receivers V_1, V_3, V_4 and V_5 (V_2 and V_3 have a symmetric behavior and then we do not show here the solution at receiver V_2 by sake of clarity) for the different values of f_c, R_c and L. The biggest errors are obtained using $f_c = 40$, $L = 10$, $R_c = 10^{-3}$, particularly for receivers V_1, V_2 and V_3. In all curves it is shown that if f_c is increased up to 100 Hz, L from 10 to 20 and R_c decreased from 10^{-3} to 10^{-5} the relative error between the reference

solution and the CPML solution is reduced and lies under a maximum threshold of around 1%. This is well summarized in Tables (1) and (2) in which velocity and density errors are provided for different values of f_c, L and R_c. Finally and as expected, solutions at receivers V_4 and V_5 which are far from or not close to the outlet solutions are almost perfect with relative errors around 0.6% lower than errors (around 0.9%) evaluated at receivers V_1, V_2 and V_3. In order to study the stability of the solution over long time periods we calculated the energy of the system $\frac{1}{2}(u^2+v^2)+(\gamma-1)\frac{p}{\rho}$ over 5 million time steps. In Figure (12), the variation of the energy of the system is shown on a semi-logarithmic scale. The energy decays very fast in the first 2 s and reaches an almost constant value as expected, which indicates that no spurious energy is injected back into the computational domain. This is another way to show the efficiency and stability of the CPML absorbing technique at long time periods and that this shifted unsplit CPML is a good candidate for fluid dynamics applications and particularly for directed flows evolving in moderately diverging geometries.

Conclusions

We introduced an unsplit convolution PML (CPML) boundary condition for the Navier-Stokes equation in the conservation form. By increasing the frequency shift f_c to values as high as 100 Hz, the PML thickness from 10 to 20 points and by decreasing the reflection coefficient R_c from 10^{-3} to 10^{-5}, the CPML becomes very efficient with no significant spurious flows propagating back into the main domain. Relative errors of the variables as different as velocities and densities reach values lower than 1 %. Furthermore, in the better case, solutions located in the corners close to the PML (receivers V_2 and V_3) or in a direction of the outflow orthogonal to the PML (receiver V_1) can reach errors lying between 0.5 % and 0.9 %. These errors are reached for f_c =100 Hz and L=20, with errors around 0.5 % for R_c=10^{-5}. Generally the parameters f_c and L are more sensitive than R_c. CPML avoids oscillations in the results and ensures stability of the whole system over long time periods of 5 million time steps. CPML is then a good candidate to build efficient absorbing boundary conditions for non linear systems like the Navier-Stokes equations. This is another argument in favor of CPML comparing to other classical or optimized PMLs. Finally this unsplit formulation allows a reduction of the number of arrays involved in the computations when it is compared to optimized or classical split PML techniques.

Acknowledgement: The authors thank Julien Diaz for fruitful discussions on the formulation of PML for fluid dynamics.

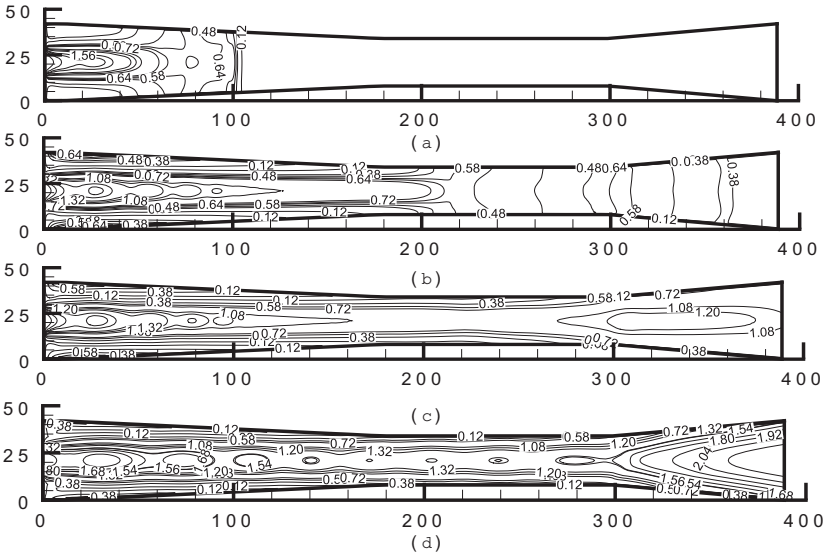

Figure 5: Snapshots of the Mach number in the ejector diffuser are reproduced at time 0.2 s, 0.9 s, 1.65 s and 5 s. The countour levels with their respective numerical labels show that compression cells are generated preferentially along the symmetry axis and that the expansion patterns at the right end are well reproduced with almost no spurious reflections coming back from the base of the PML and retropropagating into the main domain. From the base (at around $x = 300$ cm) to the end of the diverging part of the device the flow expands with an expected increase of the Mach number up to values around 2.2. As the no-slip conditions are imposed at the walls, a viscous boundary layer develops near the walls in which the flow is subsonic. At around 5 s, the flow dynamics reach an almost steady state regime after 5 million time steps. The subsonic transition layer close to the walls is not significantly perturbed even in the diverging part of the ejector and close to the PML, which is difficult to obtain. Indeed, instabilities can be generated in the subsonic layer if non improved PML are used, which is not the case here. This provides us very encouraging results and shows that our PML is a good candidate for directed flows in industrial applications.

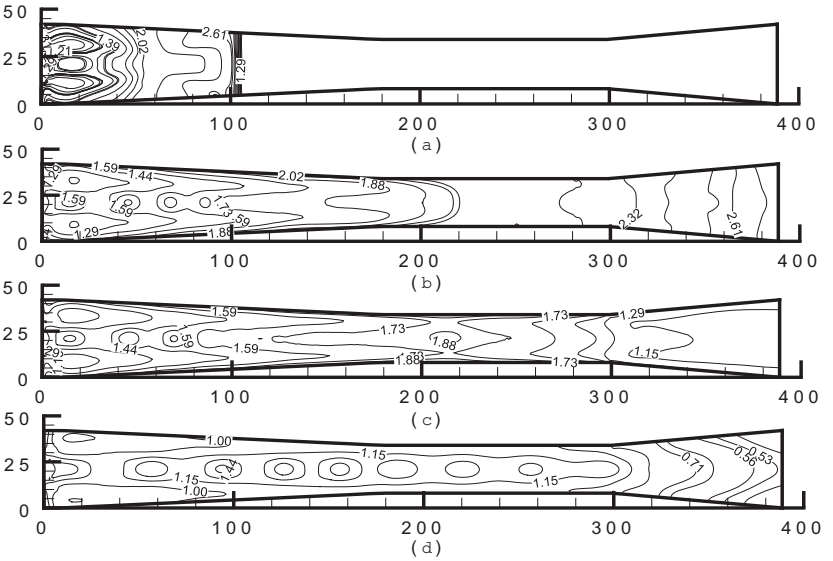

Figure 6: Snapshots of the density in the ejector diffuser are reproduced at time 0.2 s, 0.9 s, 1.65 s and 5 s. As in Figure (5), the countour levels with their respective numerical labels show that compression cells are generated preferentially along the symmetry axis and that the expansion patterns at the right end are well reproduced with almost no spurious reflections coming back from the base of the PML. From the base (at around $x = 300$ cm) to the end of the diverging part of the device the flow expands with a regular decrease of the density as expected. At around 5 s, the flow dynamics reach an almost steady state regime after 5 million time steps. The subsonic transition layer close the walls is not significantly perturbed even in the diverging part of ejector and close to the PML, which is difficult to obtain.

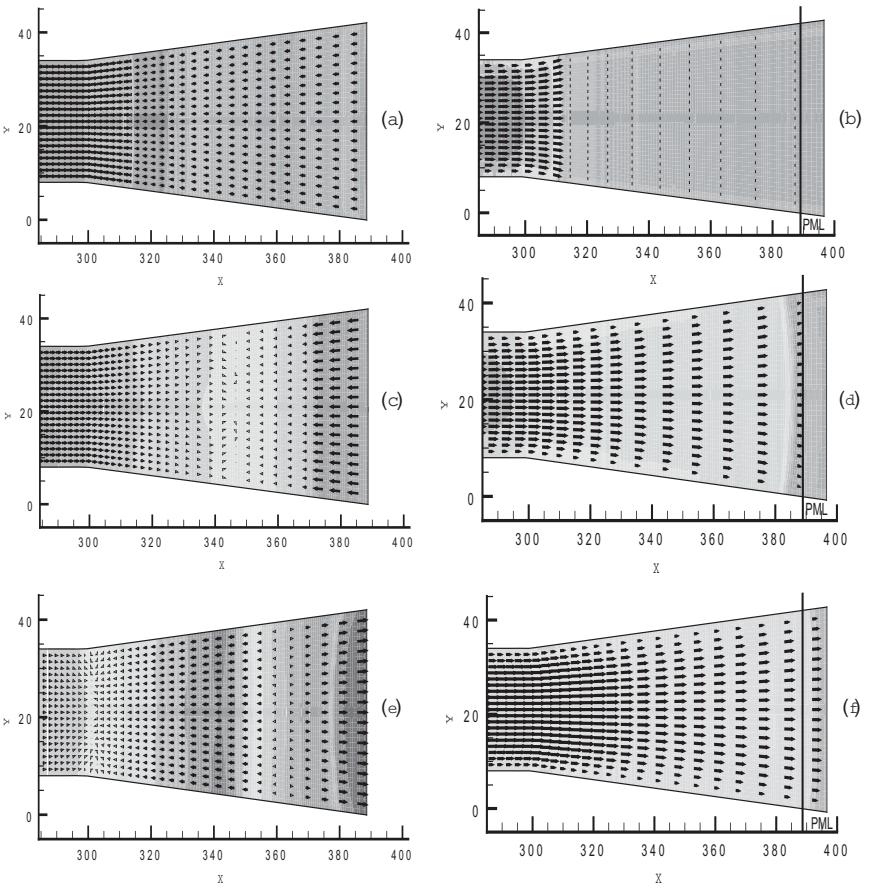

Figure 7: The velocity field is shown here at different times in a zoomed region corresponding to the right diverging part of the ejector (coordinates expressed in centimeters). It is superimposed to the Mach number. In the left column (Figures (*a*), (*c*) and (*e*)) we use standard Neumann conditions at the right oulet and we can see a strong interaction between the main flux and the spurious flux coming back from the right edge. In the right column (Figures (*b*), (*d*) and (*f*)) a PML is present at the right end of the ejector. In this case the spurious returning flux is avoided and the PML is really efficient.

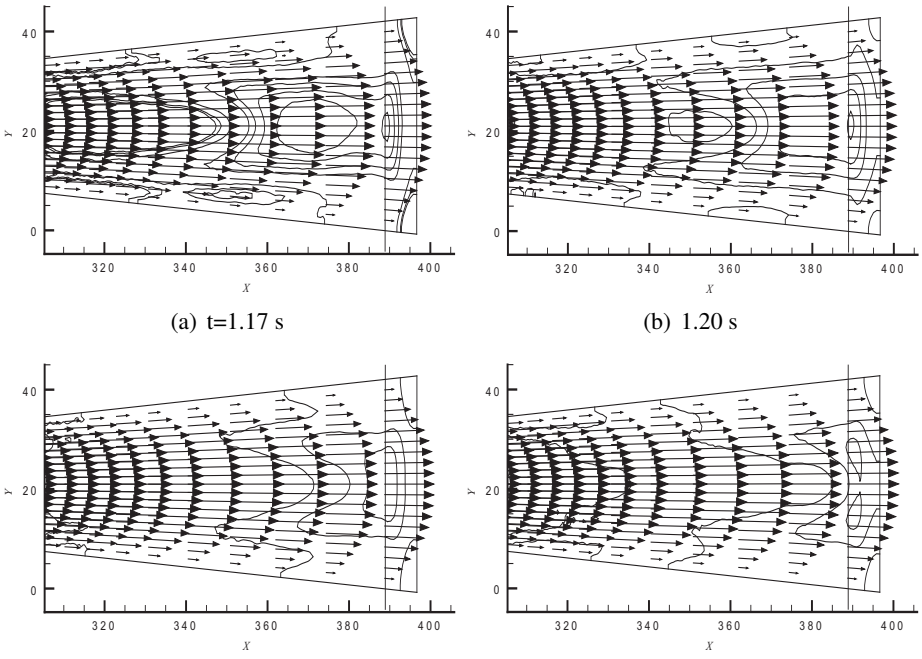

(a) t=1.17 s (b) 1.20 s

(c) 1.23 s (d) 1.26 s

Figure 8: We show here, in the same zoomed section of the ejector (coordinates expressed in centimeters) as in Figure (7), how density is efficiently absorbed in the PML region at different times.

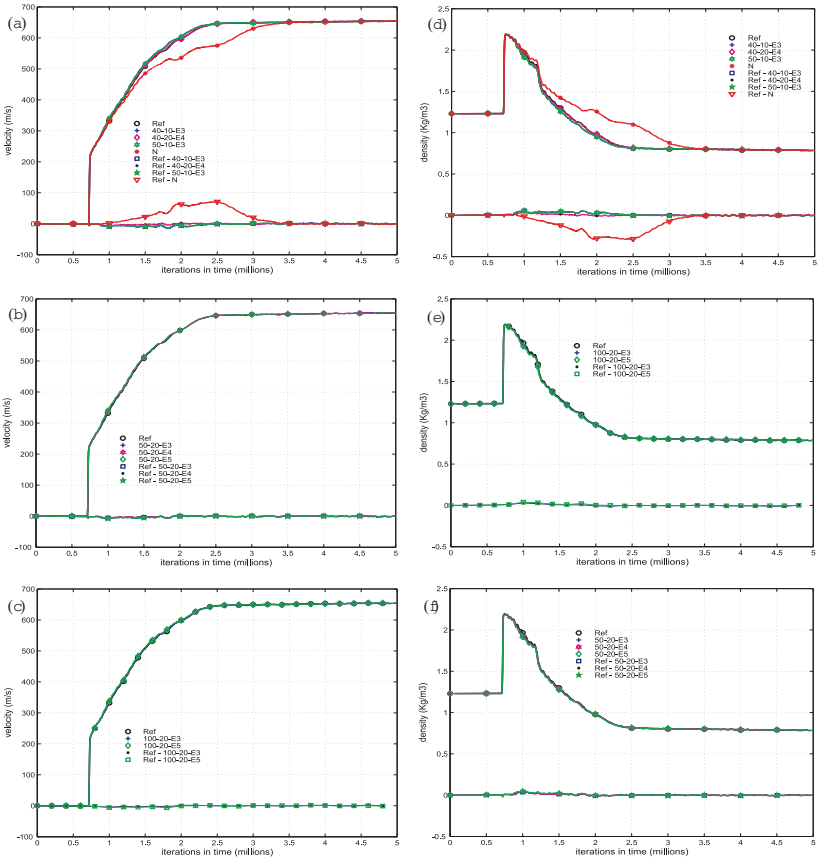

Figure 9: Horizontal velocity (left) and density (right) registered at receiver V_1 over a long time period of 5 s and for different values of the frequency shift f_c, the PML thickness L and the reflection coefficient R_c. Newmann solutions (N) are also plotted as well as the difference between the reference solution and the PML (or Newmann) solutions. In all the simulations the Newmann solutions are really bad as expected. (Left) In (a) we can observe that for $f_c = 40$ Hz and $L = 10$ points there are some discrepancies between PML and reference solutions. In (b) PML solutions are significantly improved by increasing f_c to 50 Hz and L to 20 points. The influence of different values of R_c is not really significant. In (c) PML solutions with $f_c = 100$ Hz and $L = 20$ points are even better independently of the values of R_c. PML and reference solutions are almost superimposed. It seems that values of R_c between 10^{-3} and 10^{-4} are sufficient. (Right) Density solutions are subject to similar accuracy behavior as for the PML velocity solutions. The increase of f_c and L have more influence than R_c coefficient. A R_c value of 10^{-3} seems to be also sufficient for this simulation while a cut-off frequency shift f_c around 100 Hz and a thickness of 20 points improve the solutions by a more efficient damping of the flow in the PML.

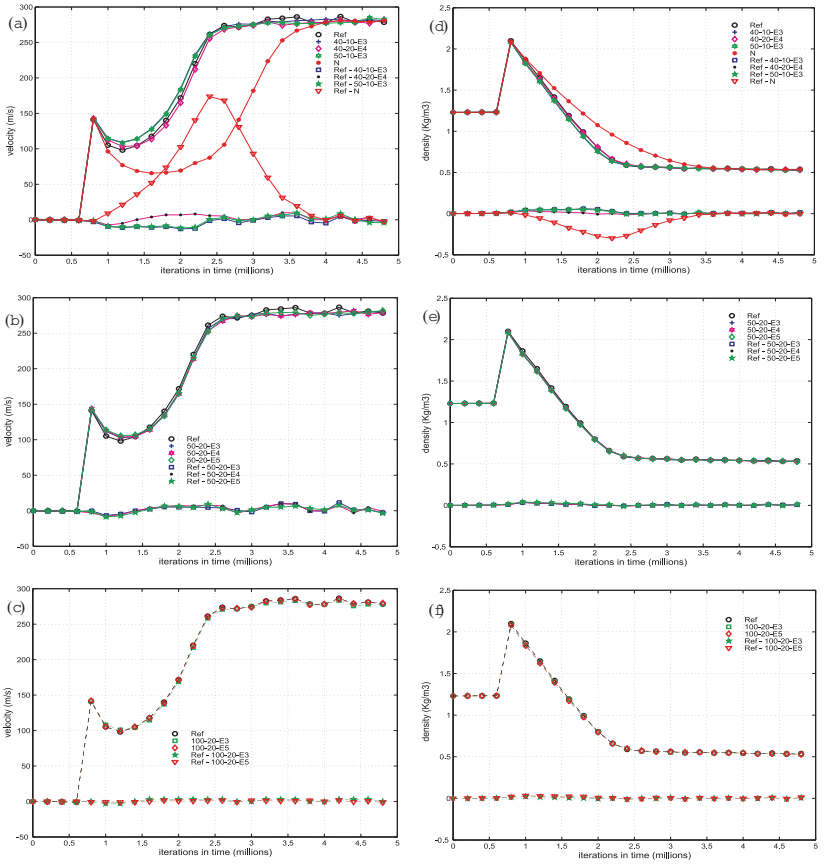

Figure 10: Same as in Figure (9) but for the receiver V_2 located at the upper corner of the right edge and close to the PML. For this particular receiver a good accuracy of the solution is much more difficult to reach than in the case of receiver V_1 because the flow is subsonic or close to subsonic at this receiver and does not impinge the PML at normal incidence but with a non zero angle. It is very interesting to notice, in particular in figures (c) and (f), the good fit between PML and reference solutions for $f_c = 100$ Hz and $L = 20$ points with almost no differences while for lower values of f_c equal to 50 Hz there are still visible discrepancies. A value of R_c equal to 10^{-5} has more significant influence in the accuracy of the solutions than a value of 10^{-3}, a value of 10^{-5} being nearly optimal. This is confirmed in the tables containing the relative errors in velocity and density evaluated at the different receivers.

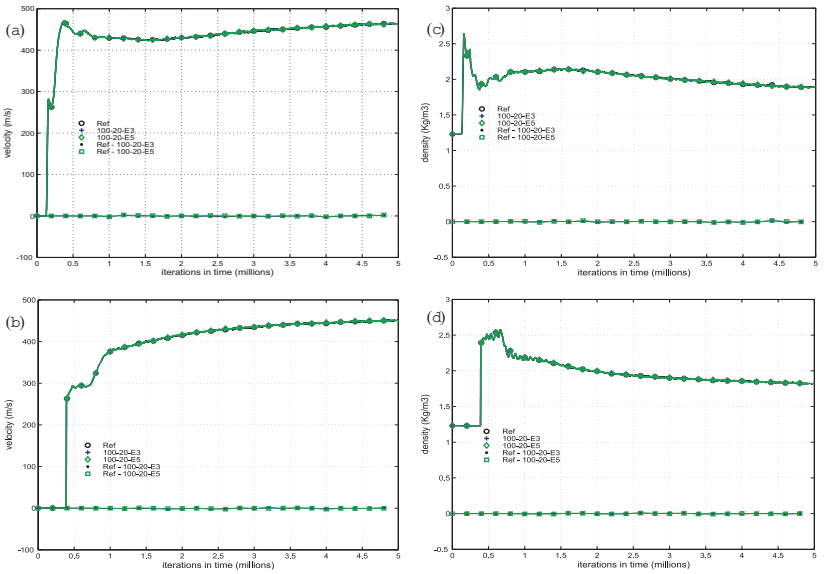

Figure 11: Evolution in time of the horizontal velocity and the density at receivers V_4 (bottom) and V_5 (top). Plot (a) shows the evolution of the horizontal component u of the velocity at receiver V_5 for $f_c = 100$ Hz, $L = 20$ points and two different values of R_c (10^{-3} and 10^{-5}). Plot (b) shows the horizontal component u of the velocity at receiver V_4 for the same parameters. Plots (c) and (d) show the evolution of the density at receivers V_5 and V_4 respectively. Both velocities and densities are very close to the reference solution with really few differences even in the density, which is more difficult to reach (see density registration in Figure (9)) . The R_c coefficient has no significant influence on the solution (a value of 10^{-3} is sufficient). The reason is that receivers V_4 and V_5 are located on the symmetry axis normal to the PML and far from the PML. The solution is excellent inside the computational domain with no contamination coming from the PML.

Table 1: We show here the velocity errors obtained at the five receivers of Figures (4), (9), (10) and (11) for different values of the cut-off frequency shift f_c (40, 50 or 100 Hz), of the PML thickness L (10 or 20 points) and of the reflection coefficient R_c (10^{-3}, 10^{-4} or 10^{-5}). The errors are also given in the case of simple and standard Newmann conditions (N) which are worse at all receivers as expected. We can observe that the lower error is obtained for $f_c = 100$ Hz, $L = 20$ and $R_c = 10^{-5}$, and particularly at receivers V_1, V_2 and V_3. The error is always lower than 1% for these optimal parameters. It is interesting to notice that really few errors are obtained (arounbd 0.5 %) at receivers V_2 and V_3 located close to the PML at non zero angle of incidence of the flow, which is more difficult to obtain than for the other receivers. This indicates that the CPML is a good candidate to absorb efficiently the flow at the outlet.

Receiver	$f_c = 100$ $L = 20$ $R_c = 1E-3$	$f_c = 100$ $L = 20$ $R_c = 1E-5$	$f_c = 50$ $L = 20$ $R_c = 1E-3$	$f_c = 50$ $L = 20$ $R_c = 1E-4$	$f_c = 50$ $L = 20$ $R_c = 1E-5$	$f_c = 50$ $L = 10$ $R_c = 1E-3$	$f_c = 40$ $L = 20$ $R_c = 1E-3$	$f_c = 40$ $L = 10$ $R_c = 1E-3$	N
V_5	0.009689	0.008650	0.008426	0.008985	0.008238	0.008816	0.008823	0.009838	0.008403
V_4	0.007668	0.007403	0.007403	0.006674	0.005970	0.005863	0.006661	0.006509	0.008168
V_3	0.010393	0.005196	0.046058	0.041419	0.040854	0.043422	0.049476	0.046823	0.610024
V_2	0.010339	0.005169	0.044532	0.044768	0.047425	0.058456	0.057800	0.044848	0.606719
V_1	0.009827	0.009434	0.010327	0.011495	0.012406	0.020091	0.022254	0.021590	0.108414

Table 2: Same study as in Table (1) but density errors are given instead of velocity errors. Density errors are given at the five receivers of Figures (4), (9), (10) and (11) for different values of the cut-off frequency shift f_c (40, 50 or 100 Hz), of the PML thickness L (10 or 20 points) and of the reflection coefficient R_c (10^{-3}, 10^{-4} or 10^{-5}). The errors are also given in the case of simple and standard Newmann conditions (N) which are worse at all receivers as expected. We can observe that the lower errors are obtained for $f_c = 100$ Hz, $L = 20$ and $R_c = 10^{-5}$ (same values as for the velocity errors in table 1), and particularly at receivers V_1, V_2 and V_3. The error is always lower than 1% for these optimal parameters. It is interesting to notice that really few errors are obtained (arounbd 0.5 %) at receivers V_2 and V_3 located close to the PML at non zero angle of incidence of the flow, which is more difficult to obtain than for the other receivers. This indicates that the CPML is a good candidate to absorb efficiently the flow at the outlet.

Receiver	$f_c = 100$ $L = 20$ $R_c = 1E-3$	$f_c = 100$ $L = 20$ $R_c = 1E-5$	$f_c = 50$ $L = 20$ $R_c = 1E-3$	$f_c = 50$ $L = 20$ $R_c = 1E-4$	$f_c = 50$ $L = 20$ $R_c = 1E-5$	$f_c = 50$ $L = 10$ $R_c = 1E-3$	$f_c = 40$ $L = 20$ $R_c = 1E-3$	$f_c = 40$ $L = 10$ $R_c = 1E-3$	N
V_5	0.006591	0.007592	0.007874	0.008503	0.007786	0.008667	0.008577	0.007507	0.008048
V_4	0.006350	0.006136	0.006074	0.005374	0.006091	0.006503	0.006304	0.007545	0.007446
V_3	0.009074	0.007730	0.018146	0.018924	0.021188	0.025788	0.027281	0.017630	0.138876
V_2	0.009330	0.007756	0.018584	0.008141	0.020328	0.026560	0.027915	0.016013	0.138626
V_1	0.009631	0.009330	0.017957	0.020881	0.023704	0.026084	0.026684	0.018114	0.134009

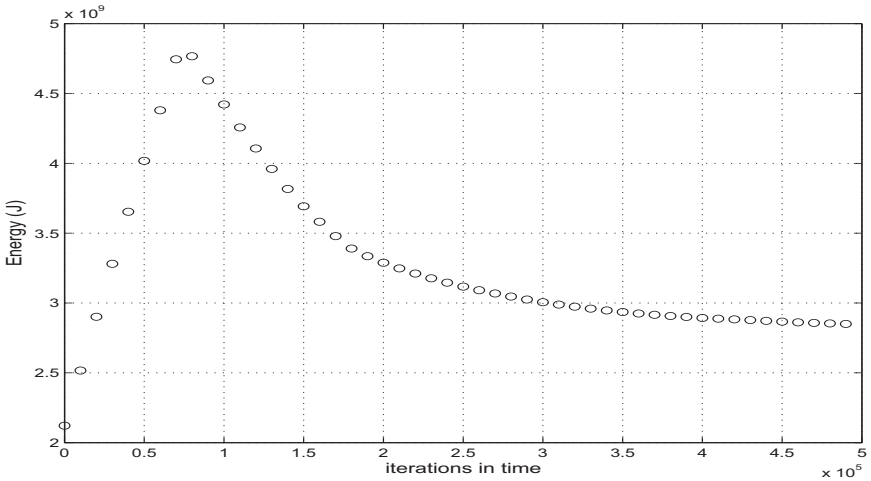

Figure 12: Evolution of the total energy in the system over long time periods. In this figure the total energy decreases very fast at around $t = 0.75$ s until it reaches a value of around 2.8×10^9 J after 5×10^6 time steps. Total energy decay evolves towards an almost constant energy at a long time period. This behavior of the energy shows the stability of our PMLs for long time periods of simulation and also the efficiency of the PMLs since no significant production of spurious energy coming back into the domain from the PML boundaries is visible.

References

Bécache, E.; Fauqueux, S.; Joly, P. (2003): Stability of Perfectly Matched Layers, group velocities and anisotropic waves. *J. Comput. Phys.*, vol. 188, no. 2, pp. 399–433.

Bérenger, J. P. (1994): A Perfectly Matched Layer for the absorption of electromagnetic waves. *J. Comput. Phys.*, vol. 114, pp. 185–200.

Chew, W. C.; Liu, Q. (1996): Perfectly Matched Layers for elastodynamics: a new absorbing boundary condition. *J. Comput. Acoust.*, vol. 4, no. 4, pp. 341–359.

Chew, W. C.; Weedon, W. H. (1994): A 3-D perfectly matched medium from modified Maxwell's equations with stretched coordinates. *Microwave Opt. Technol. Lett.*, vol. 7, no. 13, pp. 599–604.

Collino, F.; Tsogka, C. (2001): Application of the PML absorbing layer model to the linear elastodynamic problem in anisotropic heterogeneous media. *Geophysics*, vol. 66, no. 1, pp. 294–307.

Couder-Castañeda, C. (2009): Simulation of supersonic flow in an ejector diffuser using the jpvm. *Journal of Applied Mathematics*, vol. 2009.

Hagstrom, T. (2003): A new construction of perfectly matched layers for hyperbolic systems with applications to the linearized Euler equations. In Cohen, G.; Heikkola, E.; Joly, P.; Neittaanmäki, P.(Eds): *Mathematical and Numerical Aspects of Wave Propagation: Waves 2003*, Proceedings of the Sixth International Conference on Mathematical and Numerical Aspects of Wave Propagation, pp. 125–129, Jyväskylä, Finland. Springer-Verlag.

Hesthaven, J. S. (1998): On the analysis and construction of perfectly matched layers for the linearized Euler equations. *J. Comput. Phys.*, vol. 142, no. 1, pp. 129–147.

Hu, F. Q. (2001): A stable perfectly matched layer for linearized Euler equations in unsplit physical variables. *J. Comput. Phys.*, vol. 173, no. 2, pp. 455–480.

Hu, F. Q. (2005): A perfectly matched layer absorbing boundary condition for linearized Euler equation with a non-uniform flow. *J. Comput. Phys.*, vol. 208, pp. 469–492.

Hu, F. Q.; Li, X.; Lin, D. (2008): Absorbing boundary conditions for nonlinear Euler and Navier-Stokes equations based on the perfectly matched layer technique. *J. Comput. Phys.*, vol. 227, pp. 4398–4424.

Komatitsch, D.; Martin, R. (2007): An unsplit convolutional Perfectly Matched Layer improved at grazing incidence for the seismic wave equation. *Geophysics*, vol. 72, no. 5, pp. SM155–SM167.

Lie, I. (2001): Well-posed transparent boundary conditions for the shallow water equations. *Appl. Math. Math.*, vol. 38, pp. 445–474.

Luebbers, R. J.; Hunsberger, F. (1992): FDTD for Nth-order dispersive media. *IEEE Transactions on Antennas and Propagation*, vol. 40, no. 11, pp. 1297–1301.

Martin, R.; Komatitsch, D. (2009): An unsplit convolutional perfectly matched layer technique improved at grazing incidence for the viscoelastic wave equation. *Geophys. J. Int.*, vol. 179, no. 1, pp. 333–344.

Martin, R.; Komatitsch, D.; Ezziani, A. (2008): An unsplit convolutional perfectly matched layer improved at grazing incidence for seismic wave equation in poroelastic media. *Geophysics*, vol. 73, no. 4, pp. T51–T61.

Martin, R.; Komatitsch, D.; Gedney, S. D. (2008): A variational formulation of a stabilized unsplit convolutional perfectly matched layer for the isotropic or anisotropic seismic wave equation. *CMES: Computer Modeling in Engineering and Sciences*, vol. 37, no. 3, pp. 274–304.

Martin, R.; Komatitsch, D.; Gedney, S. D.; Bruthiaux, E. (2010): A high-order time and space formulation of the unsplit perfectly matched layer for the seismic wave equation using Auxiliary Differential Equations (ADE-PML). *CMES: Computer Modeling in Engineering and Sciences*, vol. 56, no. 1, pp. 17–41.

Nataf, F. (2006): A new approach to perfectly matched layers for the linearized Euler equations. *J. Comput. Phys.*, vol. 214, no. 2, pp. 757–772.

Navon, I. M.; Neta, B.; Hussaini, M. Y. (2004): A Perfectly Matched Layer approach for the linearized shallow water equations models. *Monthly Weather Review*, vol. 132, pp. 1369–1378.

Poinsot, T.; Lele, S. (1992): Boundary conditions for direct simulations of compressible flows. *J. Comput. Phys.*, vol. 101, pp. 104–129.

Thompson, K. W. (1987): Time dependent boundary conditions for hyperbolic systems. *J. Comput. Phys.*, vol. 68, pp. 1–24.

Thompson, K. W. (1990): Time dependent boundary conditions for hyperbolic systems: II. *J. Comput. Phys.*, vol. 89, pp. 439–461.